NASA Contractor Report 178294

Development of Response Models for the Earth Radiation Budget Experiment (ERBE) Sensors:

Part III – ERBE Scanner Measurement Accuracy Analysis Due to Reduced Housekeeping Data

Sang H. Choi, Dan A. Chrisman, Jr. and Nesim Halyo

Information & Control Systems, Incorporated
Hampton, Virginia 23666

Contract NAS1-16130

March 20, 1987

National Aeronautics and
Space Administration

Langley Research Center
Hampton, Virginia 23665-5225

FOREWORD

This report entitled "Development of Response Models for the Earth Radiation Budget Experiment (ERBE) Sensors" consists of the following four parts.

Part I, NASA CR-178292, is entitled "Dynamic Models and Computer Simulations for the ERBE Nonscanner, Scanner and Solar Monitor Sensors".

Part II, NASA CR-178293, is entitled "Analysis of the ERBE Integrating Sphere Ground Calibration".

This is Part III, NASA CR-178294, entitled "ERBE Scanner Measurement Accuracy Analysis Due to Reduced Housekeeping Data".

Part IV, NASA CR-178295, is entitled "Preliminary Nonscanner Models and Count Conversion Algorithms".

SUMMARY

This report entitled "Development of Response Models for the Earth Radiation Budget Experiment (ERBE) Sensors" consists of four parts. This part, Part III, NASA CR-178294, is entitled "ERBE Scanner Measurement Accuracy Analysis Due to Reduced Housekeeping Data". The remaining parts are as follows.

Part I, NASA CR-178292, is entitled "Dynamic Models and Computer Simulations for the ERBE Nonscanner, Scanner and Solar Monitor Sensors".

Part II, NASA CR-178293, is entitled "Analysis of the ERBE Integrating Sphere Ground Calibration".

Part IV, NASA CR-178295, is entitled "Preliminary Nonscanner Models and Count Conversion Algorithms".

The scanner model introduced in Part I is based on the initial design of the instrument. In this design, housekeeping data was sampled every scan, i.e. every four seconds. During the ground calibrations for the NOAA-9 Proto Flight Model (PFM), error analysis revealed that sampling the HK data this often generated random noise which interfered with the scanner radiometric signal (Reference 1). To minimize the interference, the instrument's hardware was modified. The frequency of HK data sampling was reduced to one every 8 scans (every 32 seconds).

This document considers the accuracy of the scanner measurements when the HK sampling frequency is reduced. The reduction of the HK data sampling frequency would provide more uncertainty for modeling the calibration sources. This uncertainity would be greatest for sources whose temperatures change rapidly or drastically. In this analysis, we focus on the MAM baffle and plate and scanner baffle due to their relatively high temperature changes during solar calibrations. Since only solar simulator data was available, we approximated the solar temperatures on these components and the radiative and thermal gradients in the MAM baffle due to reflected sunlight.

Simplified models for the MAM baffle and plate and scanner baffle were made to account for any instantaneous radiation field changes within the field-of-view of a scanner instrument during a solar calibration. The channel selected for analysis was the total wavelength channel of the scanner instrument.

The simplified model yields instantaneous solar radiance (L) and emitted radiant flux (E_{FOV}) from the MAM baffle and plate and scanner baffle while they are subject to an instantaneously changing solar flux angle and a relatively slow chaning mode of environments in an orbit operation.

With a solar flux angle change the MAM has a partial or a full view of the sun, and the MAM baffle has exterior and interior exposures. Due to this change, the effects on the radiation fields at the scanner baffle field-of-view are apparent. The environmental conditions such as cold and hot orbits (-10° ~ 30° C) and sun-blips (day and night, in this case, the earth albedo is changed), are not influential in a relative sense as compared with solar flux changes (i.e., shadow and exposure). Nevertheless, the environmental impacts were considered in a simplified model to prove these conditions to be negligible.

The models were used for two different cases. The one case is TRY-I which uses the measured MAM plate and baffle temperatures obtained from the ground calibration, and the other case is TRY-II which uses the MAM plate and baffle temperatures computed from the MAM baffle model.

In both TRY-I and II cases, the temperature increments during an increasing partial (60 seconds) through a full (210 seconds) to a diminishing partial sun-view were 2.75°K and 9°K, respectively. During one scan cycle in a full sun-view, the solar radiance increments are about 0.055 $W/m^2 \cdot sr$ for TRY-I case and 0.17 $W/m^2 \cdot sr$ for TRY-II case. These results are due to the longwave contributions reflected and emitted from the MAM plate and baffle.

The scanner simulation model, when it was coupled with TRY-I and II cases, shows that the count output increments are about 1 count for TRY-I and about 1.5 count for TRY-II. These count increments are equivalent to about 0.17 $W/m^2 \cdot sr$ and 0.26 $W/m^2 \cdot sr$ radiance increments respectively, if 1 $W/m^2 \cdot sr$ is equivalent to 6 counts. In this computation, the scanner simulation model was integrated with the scanner baffle model. The differences would be due mainly to the emitted radiant flux E_{FOV} from the scanner baffle. The radiance equivalent to the emitted radiant flux increment, ΔE_{FOV}, from the scanner baffle was about 0.09 $W/m^2 \cdot sr$ per scan cycle. The emitted radiant flux E_{FOV} from the scanner baffle was estimated by setting the MAM plate and baffle temperature at 283.16°K.

Accordingly, eliminating the ΔE_{FOV} effect which is about 0.55 counts from the results from the scanner simulation model coupled with TRY-I and II, the real count output increments per scan cycle are 0.45 and 0.95 counts for TRY-I and II, respectively. Because the count difference between the source and spacelooks is used in the count conversion procedure, the elimination of E_{FOV} which is almost the same during a scan period would not cause any significant errors.

As a whole, any difference attributed to the MAM plate and baffle temperature variations has a negligible effect on the input radiation field impinging on the instrument field of view limiter.

The results from the above analysis show that the unaccountable solar radiance and irradiance variations during a scan cycle are small.

Hence, it is certain that any reasonable interval longer than current HKD acquisition interval (every 4 seconds) will not significantly affect the estimation of a radiation field at the field of view of a scanner instrument unless unknown factors disturb the radiation field and thermal loadings.

TABLE OF CONTENTS

LIST OF FIGURES

LIST OF TABLES

LIST OF SYMBOLS

Symbol	Definition
A_c	Area of rectangular shape baffle cross-section
A_M	MAM FOV area
E_{FOV}	Emitted radiant flux
E_{SUN}	Solar flux
E_b	Radiant inicidence at barrel
E_{SOURCE}	Source irradiance change during the day and night
H	Height of barrel
h	Height of barrel less exposure area height, l
k	Thermal coupling
l	Height of an exposure area at angle ϕ
L	Instantaneous solar radiance
P_M	Total power a MAM plate can receive
P	Perimeter of rectangle shape baffle cross-section
R	Radius of MAM cylinder at any point along the z-axis
R_D	Radius of MAM barrel
R_M	Radius of MAM barrel openings
Sr	Steradian
S	Distance between two infinitessimal areas on the MAM plate
T_b	Instantaneous barrel temperature
T_{sc}	Spacecraft temperature

LIST OF SYMBOLS (CONCLUDED)

Symbol	Definition
α_b	Baffle exterior surface radiation parameters
εb	Baffle exterior surface radiation parameters
η_M	Attenuation factor of the MAM
θ	Solar flux angle WRT the baffle entrance
ρ_M	Reflectivity of MAM
σ	Stefan-Boltzmann constant
ϕ	Azimuth angle
Ω	Solid angle, baffel barrel

Additional Symbols Defined For:

LIST OF ACRONYMS

Acronym	Definition
A/D	Analog-to-Digital (conversion)
FOV	Field-of-View
HKD	Housekeeping Data
MAM	Mirror Attenuator Mosaic
MAX	Maximum
NOAA	National Oceanic and Atmospheric Administration
PFM	Proto Flight Model

MAM FOR A SOLAR CALIBRATION

1. GENERAL DESCRIPTION

The mirror attenuator mosaic (MAM) for solar calibration was designed to guide and attenuate the solar flux impinging into the scanner instruments. To do that the baffles were put in front of the MAM to guide and limit the solar flux within a given field-of-view. The minimum acceptance field-of-view of the MAM by the baffles is about 7.1° and the length of the MAM assembly including baffles is about 4 times longer than the scanner instrument (see Fig. 1). Therefor, the exposure of the baffle to the solar flux would be an apparent consequence. The baffle heated by solar flux would be a source contributing longwave radiation to the scanner. This longwave source, accordingly, must be considered in modeling the MAM.

2. SOLAR RADIANCE

The solar flux which passes through the baffle barrel and MAM is obtained by considering baffle barrel solid angle, Ω, and the attenuation factor, η_M, of MAM.

Let $E_{sun}[\theta(t), \phi_o]$ be a solar flux at MAM baffle FOV, the solar radiance through MAM can be calculated by

$$L_M = E_{SUN}[\theta(t), \phi_o]\ (1-\eta_M)A_M(t)/(A_M\Omega) \qquad (1)$$

where the solar flux $E_{SUN} = 0.1351\ W/cm^2$

the solid angle $\Omega = \pi$ sr.

the MAM FOV area $A_M = 20.912\ cm^2$

The attenuation factor, η_M, was not characterized, however an estimated value of 30% was used.

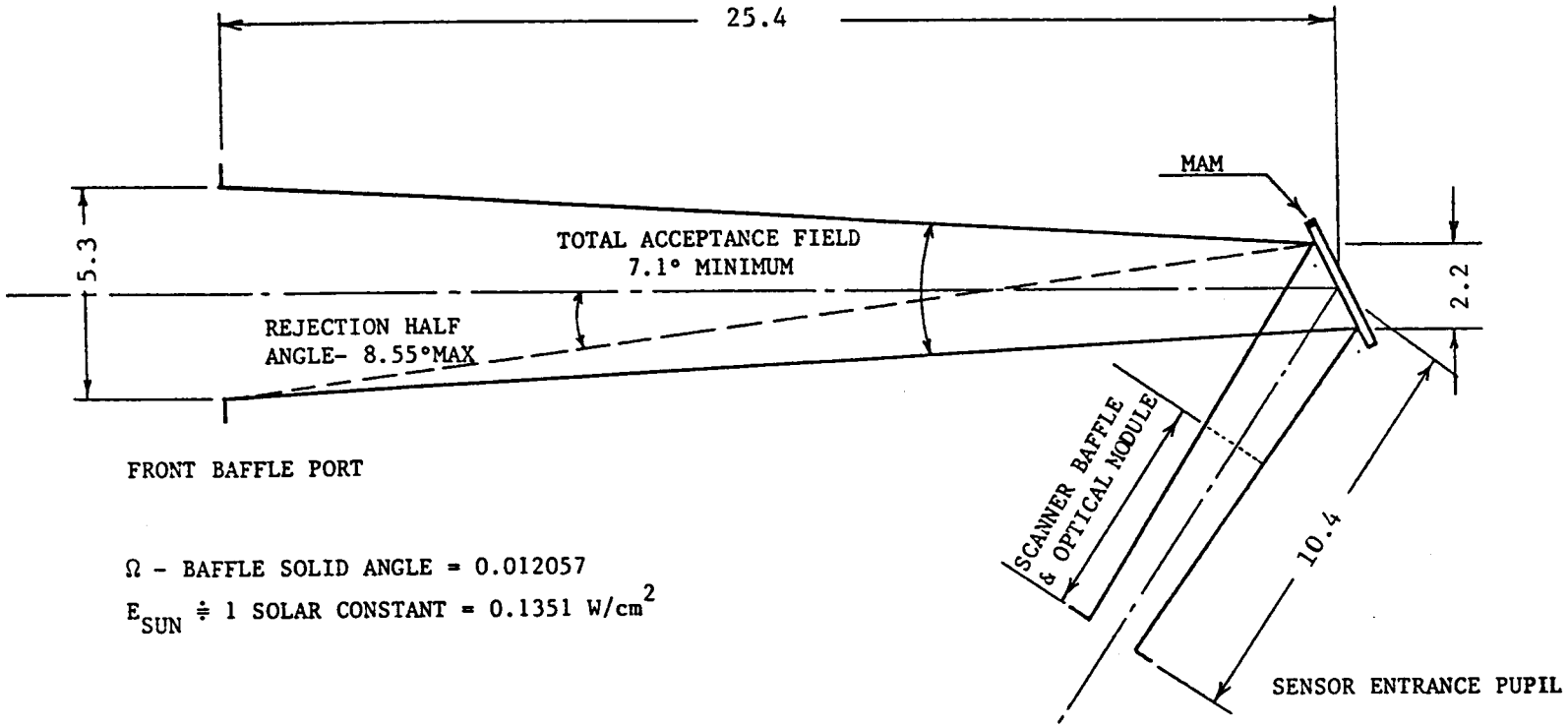

Figure 1. MAM Elevation Baffling. (Dimensions in cm)

3. LONGWAVE CONTRIBUTIONS

3-1. From MAM Baffle

The longwave contribution from the MAM baffle can be defined by knowing the exposure area, the solar flux angle, the instrument orientation in the orbit, and etc...

Consider that the interior of the baffle barrel has a diffuse black surface and the outside of the baffle barrel is exposed to the solar flux. In fact, the outside and inside surfaces of the baffle barrel are subject to the instantaneous heating due to their solar exposure. The baffle temperature is monitored by two temperature probes attached on the baffle barrel. The MAM plate also has two temperature probes.

Accounting for the solar heating of the MAM baffle is very difficult because of the configuration of the MAM baffle and the thermal influence from the spacecraft due to the conductively coupled situation. Hence, some assumptions are necessary to simplify the modeling of the MAM baffle. First consider that the solar heating of the MAM baffle barrel by the exterior exposure is very small because the exterior surface of the MAM baffle is coated with a highly reflective material. That is, the reflectivity of the surface is near to unity, so that the solar heating through the exterior for the period of solar flux measurement, which is a relatively short period of time as compared to the time constant of the MAM baffle, has little effect on the MAM baffle temperature. However, the minimal amount of the solar heating through the exterior can be compensated by considering a correction term to the interior heating.

Second, assume that the MAM baffle has a cylindrical channel although the actual channel is a square tube with rounded corners. This assumption gives an axis of symmetry which enables the model to accommodate the sunlight shadow nicely.

Let also the baffle barrel interior be flat, then the configuration of the barrel under these assumptions becomes a simple cylindrical shape. The interior of the baffle barrel is regarded as a near-perfect black surface. Therefore, the flat interior wall assumption will not make any significant difference in the radiation exchange pattern because of its low reflectivity. With these assumptions, the following figure (Fig. 2) is made for the modeling purpose: the dotted area is the exposure area where the sunlight passes through the MAM baffle FOV. The radius of the barrel can be determined by the following definition. At the bottom plane which has a rectangle shape,

$$R_D = \frac{2^* \text{ (area of rectangle shape baffle cross-section)}}{\text{Perimeter}}$$

$$= \frac{2A_c}{P} .$$

The radius of the cylinder at any point on the Z-axis is

$$R = R_D + (H - \frac{\ell}{2}) \tan 0.062. \tag{2}$$

The dotted area is

$$A[\theta(t), \phi] = 2R\ell_{max}. \tag{3}$$

As shown in the Figure 2, the position of the sun relative to the MAM baffle barrel is always changing during solar measurement. The angle, θ, that is, the solar flux angle with respect to the baffle entrance opening plane, varies from zero to π while the azimuth angle ϕ remains unchanged. The azimuth

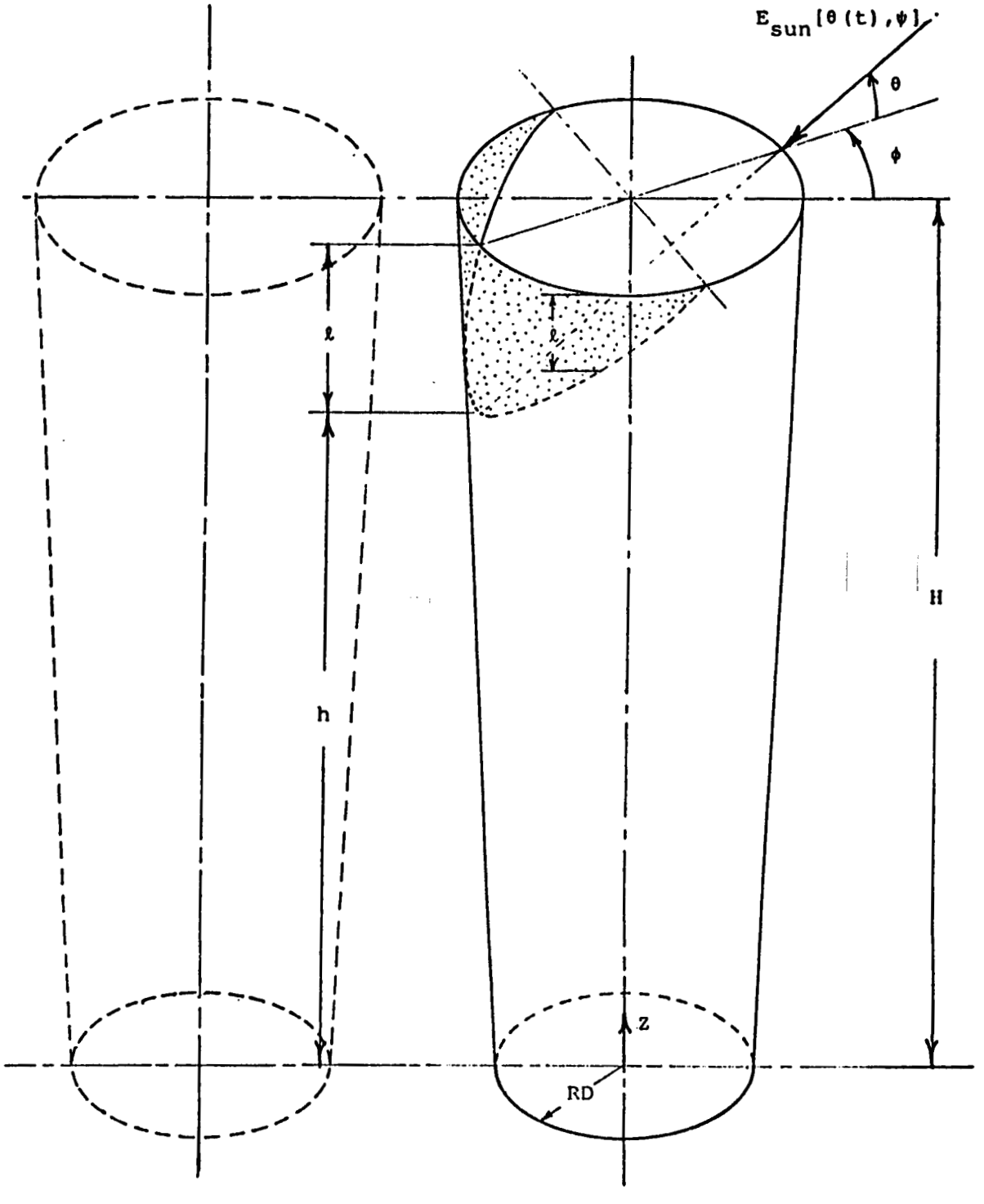

Figure 2. MAM plates and baffles for the shortwave and total scanner instruments.

angle ϕ is not an important factor unless each scanner instrument shares a MAM plate. Therefore, describing the area as a function of θ, the equation 2 becomes

$$A[\theta(t), \phi] = 4R^2 \tan \theta(t). \tag{4}$$

The height of an exposure area at an arbitrary angle ϕ can be described in the form

$$\ell = 2R \tan \theta \cdot \cos(\pi+\phi_o - \psi) \tag{5}$$

where $\psi=\phi_o + \phi$.

Differentiating (5) yields

$$d\ell = 2R \frac{1}{\cos^2\theta} \cos(\pi+\phi_o - \psi)\, d\theta.$$

As the radiant energy leaving the exposure area travels towards the MAM plate, the total power that the MAM plate can receive is described by

$$P_M = \frac{1}{\pi} \int_{A_1} \int_{A_2} E_b\ (\theta,\psi)\ \frac{\cos\beta_1\ \cos\beta_2}{S^2}\ dA_2 dA_1$$

where $E_b(\theta,\psi) = E_b = \sigma T_b^4$

since the baffle barrel interior is regarded as a blackbody. Thus, the radiant incidence from A_2 to A_1 becomes

$$E_1 = \frac{E_b}{\pi A_1} \int_{A_1} \int_{A_2} \frac{\cos\beta_1\ \cos\beta_2}{S^2}\ dA_2\ dA_1\ . \tag{6}$$

The variables within the above integral are defined based on the depiction on Fig. 3 as follows:

the infinitesimal areas on the MAM plate and the exposure, respectively, are

$$dA_1 = r\, dr\, d\psi_1,$$

$$dA_2 = R\, d\ell\, d\psi_2 = \frac{2R^2}{\cos^2\theta} \cos(\Pi+\phi_o - \psi_2)\, d\theta\, d\psi_2$$

and the distance S between two infinitesimal areas is

$$S^2 = (H - \tfrac{\ell}{2})^2 + R^2 + r^2 - 2Rr\cos(\psi_2 - \psi_1).$$

The angles between normals to the infinitesimal areas and S are

$$\cos\beta_1 = \frac{(H - \frac{\ell}{2})}{S}$$

and

$$\cos\beta_2 = \frac{\cos(0.062)}{2RS}\left[\left(\frac{R}{\cos(0.062)}\right)^2 + S^2 - (H - \tfrac{\ell}{2} + R\tan(0.062))^2\right].$$

Therefore, the integral F_{1-2} becomes

$$F_{1-2} = \frac{1}{\Pi A_1}\int_o^{2\Pi}\int_o^{R_D}\int_{\phi_o + \frac{1}{2}\pi}^{\phi_o + \frac{3}{2}\pi}\int_o^{\theta_{max}} \frac{R\cos(\Pi+\phi_o - \psi_2)\,(H - \frac{\ell}{2})}{\cos^2\theta\, S^4}$$

$$\cdot\, [(\frac{R}{\cos(0.062)})^2 + S^2 - (H - \tfrac{\ell}{2} + R\tan(0.062))^2]\, d\theta\, d\psi_2\, dr\, d\psi_1 \cdot \qquad (7)$$

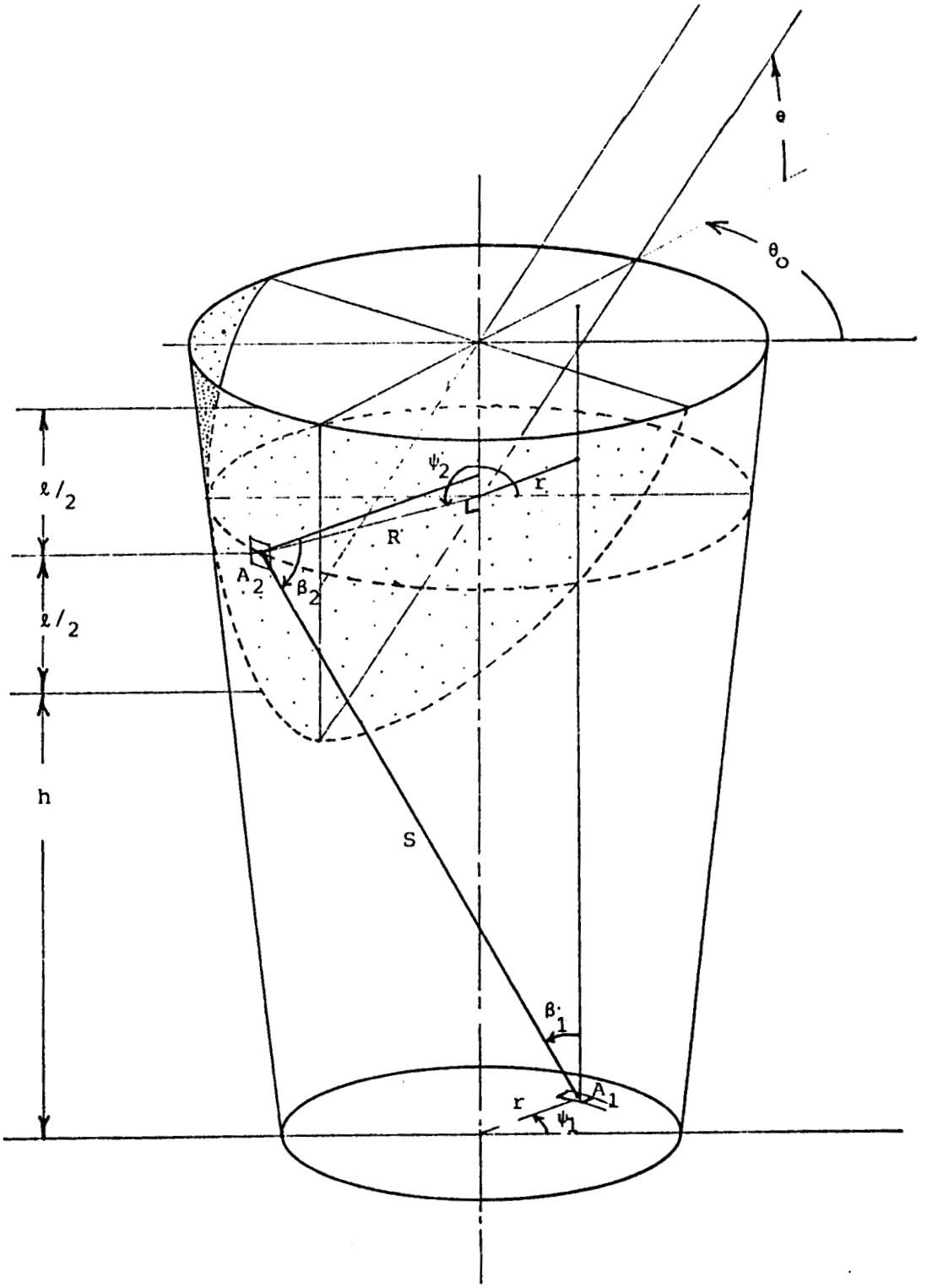

Figure 3. A general view of solar exposure area on the MAM baffle interior surface.

The max solar angle θ_{max} can be determined by

$$\theta_{max} \doteq \tan^{-1} \frac{\ell_{max}}{R_D + H \cdot \tan(0.062)} \quad . \tag{8}$$

For convenience, let's select ℓ_{max} based on the height of the barrel. That is,

$$\ell_{max} = nH, \qquad n = 1, 2, 3, \ldots$$

However, when the exposed area exceeds the height of the barrel, the view factor defined as above cannot be applied in the analysis. Accordingly, the case is limited to using ℓ_{max} by n=1.

3-2. From MAM Plate

When $n \geq 1$, then the MAM plate is subjected to solar flux. Solar flux on the MAM plate gradually evolves to cover the whole area, then diminishes away. During the time, the longwave contribution due to the increase in local MAM plate temperature and the solar power through the MAM would vary as a function of solar angle θ.

The Figs. 4 and 5 show the exposure area of a MAM plate at a certain angle $\theta(t)$. In this case, the baffle barrel and MAM have the areas partially heated by the sunlight exposure.

Consider that the angle α_D is between 0 and $\pi/2$, that is

$$0 \leq \alpha_D \leq \frac{\pi}{2} \quad .$$

In this overlapped portion of two circles shown in Fig. 5,

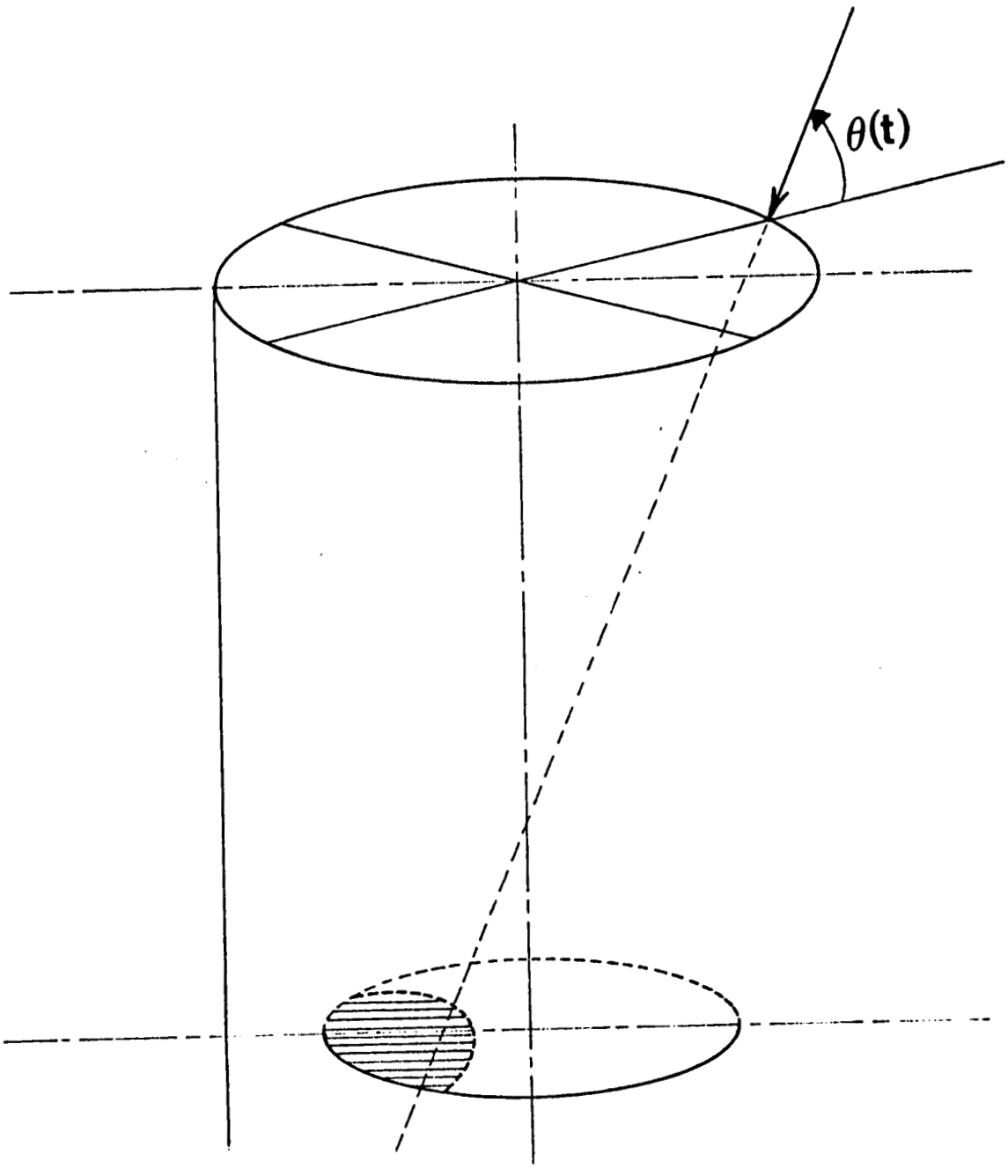

Figure 4. A partial image of the sun on the MAM plate.

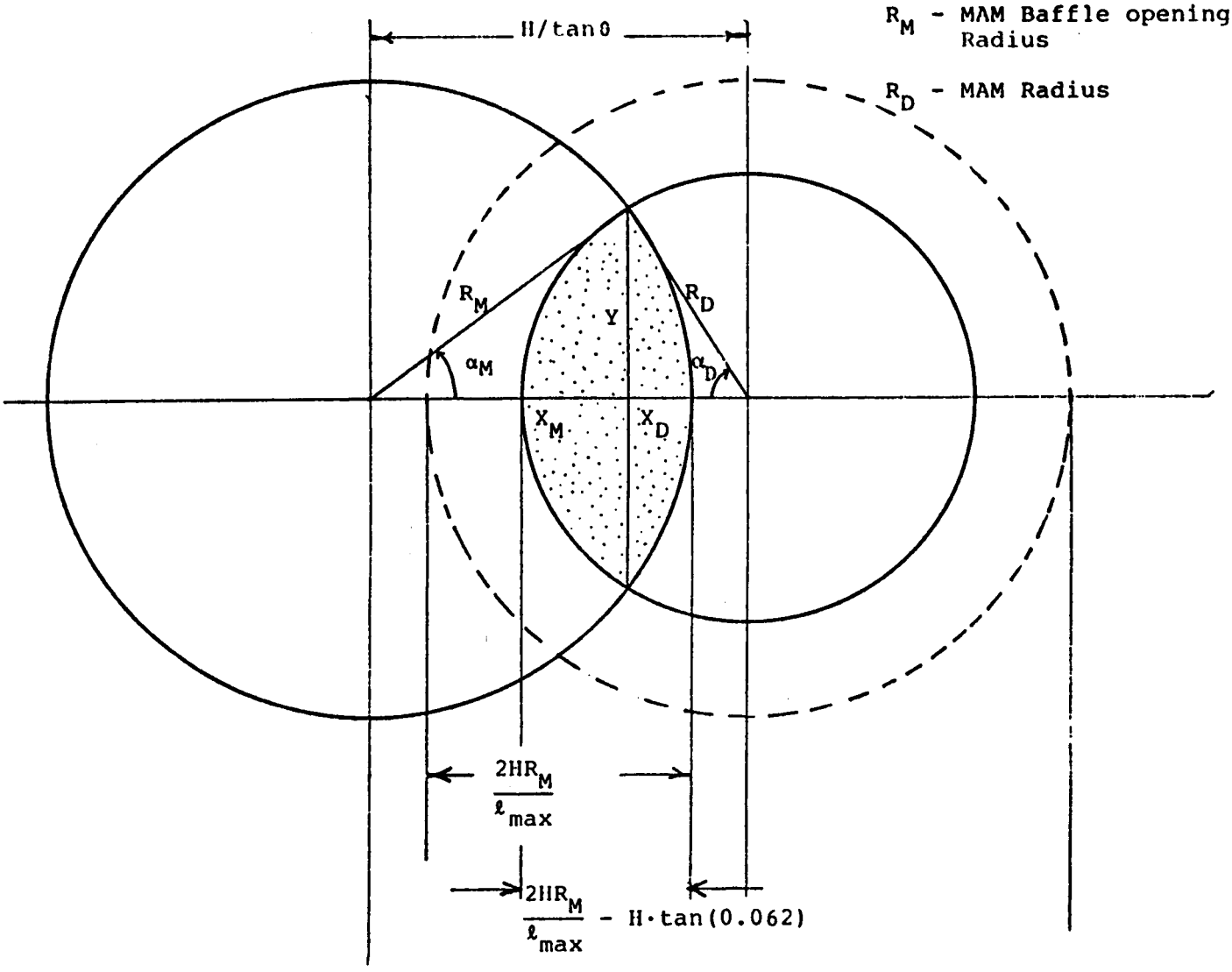

$$R_M^2 = X_M^2 + Y^2$$

$$R_D^2 = X_D^2 + Y^2$$

$$X_M + X_D = H/\tan\theta$$

Figure 5. A partial sun-view when $0 \leq \alpha_D \leq \frac{\pi}{2}$.

$$X_D = \frac{\tan\theta}{2H}\left(\frac{H^2}{\tan^2\theta} - R_M^2 + R_D^2\right)$$

$$X_M = \frac{H}{\tan\theta} - \frac{\tan\theta}{2H}\left(\frac{H^2}{\tan^2\theta} - R_M^2 + R_D^2\right)$$

$$Y = \left\{R_D^2 - \frac{\tan^2\theta}{4H^2}\left(\frac{H^2}{\tan^2\theta} - R_M^2 + R_D^2\right)^2\right\}^{\frac{1}{2}}.$$

Thus, using the above values, the angles α_M and α_D are determined by

$$\alpha_M = \cos^{-1}\frac{X_M}{R_M}$$

$$\alpha_D = \cos^{-1}\frac{X_D}{R_D}.$$

The exposure is

$$A(t)_{MAM} = A_M + A_D$$

$$= \alpha_M R_M^2 + \alpha_D R_D^2 - (X_M + X_D)\,Y$$

$$= \alpha_M R_M^2 + \alpha_D R_D^2 - \frac{H}{\tan\theta(t)}Y. \qquad (9)$$

When

$$\frac{\Pi}{2} < \alpha_D < \Pi,$$

$$X_D = \frac{\tan\theta(t)}{2H}\left(R_M^2 - R_D^2 - \frac{H^2}{\tan^2\theta(t)}\right)$$

$$X_M = \frac{H}{\tan\theta(t)} + \frac{\tan\theta(t)}{2H}\left(R_M^2 - R_D^2 - \frac{H^2}{\tan^2\theta(t)}\right)$$

$$Y = \left\{R_D^2 - \frac{\tan^2\theta(t)}{4H^2}\left(R_M^2 - R_D^2 - \frac{H^2}{\tan^2\theta(t)}\right)^2\right\}^{\frac{1}{2}}$$

and

$$\alpha_M = \cos^{-1}\frac{X_M}{R_M}$$

$$\alpha_D = \Pi - \cos^{-1}\frac{X_D}{R_D} \quad .$$

The exposure area

$$A(t)_{MAM} = \Pi R_D^2 - (\Pi - \alpha_D)\, R_D^2 + X_D Y + \alpha_M R_M^2 - X_m Y$$

$$= \alpha_D R_D^2 + \alpha_M R_M^2 - (X_M - X_D)\, Y$$

$$= \alpha_D R_D^2 + \alpha_M R_M^2 - \frac{H}{\tan\theta(t)}\, Y \quad . \qquad (10)$$

When $\theta(t) = \Pi/2 - 0.062$, namely, the MAM plate is completely filled with sunlight, the full view period is determined by

$$\frac{\Pi}{2} - 0.062 \le \theta(t) \le \frac{\Pi}{2} + 0.062.$$

In such a case, the baffle area exposed to the sunlight is simply determined by

$$A_{exp} = \Pi[(R_D + H\cdot\tan(0.062))^2 - R_D^2]. \qquad (11)$$

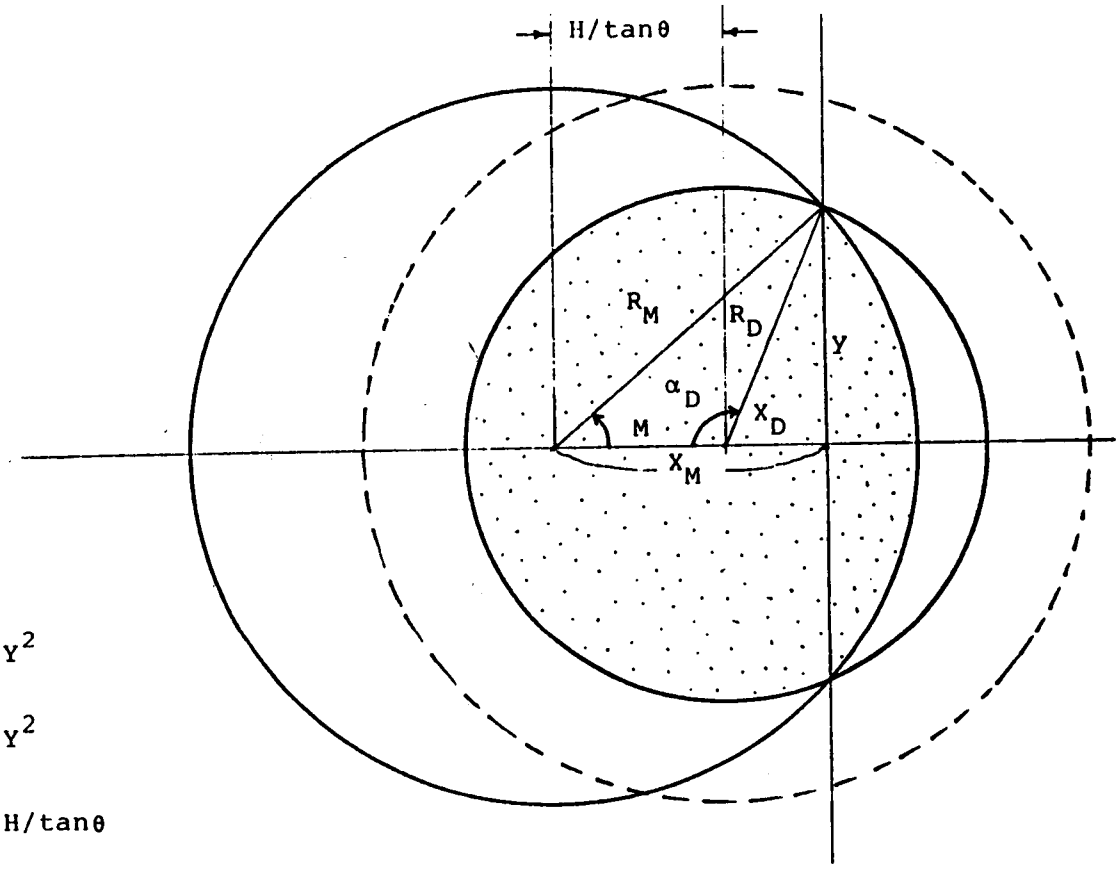

$$R_M^2 = X_M^2 + Y^2$$

$$R_D^2 = X_D^2 + Y^2$$

$$X_M - X_D = H/\tan\theta$$

Figure 6. A partial sun-view when $\pi/2 < \alpha_D < \pi$.

The next pages show a couple of approaches to approximately solve the long-wave contribution and find the attenuated beam intensity after MAM reflection. The MAM and baffle temperatures were linearly approximated based on the measurement results. The MAM exposure area was also linearly approximated to accomodate the partial and full views during the solar calibration, although a method was developed to compute those exposure areas with respect to time.

4. ROUGH ESTIMATION OF THE SOURCE RADIANCE

The solar radiance from the MAM is a combination of solar flux reflected from MAM and the emitted fluxes from MAM baffle barrel and plate. As a first try, consider that the MAM baffle and plate temperatures are linearly varied as observed from measurement results while solar calibration is performed. Considering that the exposure area of MAM varies from a partial view (1 minute), through a full view (3.5 minutes) to a final partial view (1 minute), the following approaches describe the emitted radiant fluxes from the MAM plate and baffle based on their temperatures under the quasi-simulated conditions of a solar calibration.

4-1. TRY-I:

(1). From MAM baffle:

$$E_{Mb}(t) = F_{1-\omega}\, \varepsilon_{\omega} \sigma\, T^{4}_{Mb}(t) \tag{12}$$

where

$$T_{Mb}(t) = 0.5\, \frac{t}{60} + 283.16$$

$$o \leq t \leq 240.$$

(2). From MAM Plate:

$$E_M(t) = \varepsilon_M \sigma T_M^4(t) \tag{13}$$

where

$$T_M(t) = \frac{1}{7}\left(\frac{t}{60}\right) + 283.16$$

$$0 \leq t \leq 240 \ .$$

(3). Directly impinging solar radiance:

$$L_M(t) = E_{sun} \cdot \eta \cdot \rho_M \, A_M(t) / (\Omega \cdot A_M) \tag{14}$$

where

$$A_M(t) = C(t) \, A_M$$

for $0 \leq t \leq 60$ sec, $\quad C(t) = \frac{t}{60}$

for $61 \leq t \leq 270$ sec, $\quad C(t) = 1$

for $271 \leq t \leq 330$ sec, $\quad C(t) = 5 - \frac{t-30}{60}$.

(4). Total Radiance

The total radiance from the MAM during a solar calibration is the summation of the above three different cases. The total radiance is regarded as a source radiance for the instrument simulation model.

$$L(t) = L_M + E_M(t)/\pi + \rho_M \, E_{Mb}(t)/\pi \tag{15}$$

The total radiance defined above would affect the change in scanner baffle temperature while it is falling into the scanner. Accordingly, the total radiance obtained above can be used in computing the instananeous temperatures of the scanner baffle which is defined later. A parameter used in the equation determining the scanner baffle temperature is,

$$E_{source} = \pi \cdot L(t).$$

(5). Parameters used in the above equations:

ε_{ω} = emissivity of MAM baffle barrel interior (0.98),

ε_{M} = emissivity of MAM plate (0.25),

ρ_{M} = reflectivity of MAM plate (0.9),

Ω = solid angle (3.141519),

σ = Stefan - Boltzmann constant (5.6697×10^{-8} W/m^2K^4),

$F_{1-\omega}$ = view factor between MAM plate and baffle (0.984),

E_{SUN} = solar flux (1351 W/m^2),

A_{M} = area of MAM plate (0.000384 m^2) .

4-2. TRY-II:

The next approach is to use a more sophisticated model to determine the MAM baffle temperature while the MAM baffle is subject to the solar heating. The approach used here is more analytical than using linear approximation of measured data for MAM baffle temperature as was done in TRY-I. In the same manner, the results from this approach are used to compute the input source radiance and the temperature of the scanner baffle.

The equation for MAM baffle temperature variation was formulated by a lumped linear approximation. Consider that the MAM baffle has a solar radiation, radiation exchange with other parts of the MAM and the spacecraft, and thermal conduction with the spacecraft frame and linearizing the radiation term, then the equation has the following form:

$$\dot{T}_{Mb} = P\, T_{Mb} + Q \tag{16}$$

where

$$P = -\frac{kA}{L} + (A_B\, F_{B-M}\, F_{B-M}\, \rho_M^{-A_o}\, F_{0-B}\, \varepsilon_{int} - A_{ext}\, \varepsilon_{ext} - A_M\, F_{M-B})\, 4\, \sigma\, T_{sc}^3$$

$$Q = \frac{kA}{L}\, T_{sc} + (A_{int}\, \alpha_{int} + F_{B-M}\, \rho_M\, A_B)\, E_{sun} + \frac{A_{ext}}{2}\, \alpha_{ext}\, \varepsilon_{sc}\, \sigma\, T_{sc}^4 + F_{B-M}\, A_B\, \varepsilon_M\, \sigma\, T_M^4 + (A_o\, F_{o-B}\, \varepsilon_{int} + A_{ext}\, \varepsilon_{ext} + A_M\, F_{M-B} - A_B\, F_{B-M}\, F_{M-B}\, \rho_M) 3\, \sigma\, T_{sc}^4 .$$

The solution to the equation is

$$T_{Mb} = (T_{sc} + \frac{Q}{P})\, e^{Pt} - \frac{Q}{P} . \tag{17}$$

The energy flux incident on the MAM plate is

$$E_{Mb} = F_{M-b} \cdot \varepsilon_{int}\, \sigma\, T_{Mb}^4 , \tag{18}$$

and the incident radiant flux increment is

$$E_{Mb} = F_{M-b}\ \varepsilon_{int}\ \sigma\ (T_{Mb}^4 - T_{sc}^4). \quad (19)$$

The parameters used for the analysis are the following:

σ = the Stefan-Boltzmann constant (5.0097×10^{-8} W/m^2,K^4)

T_{sc} = orbit-dependent spacecraft temperature (283.16°K)

ρV = the mass of MAM baffle barrel (1680.5 gr)

c = the specific heat of MAM baffle material (0.9 J/gr·K)

k = the thermal conductivity of MAM baffle material (1.56 W/cmK)

A = the area of conduction (0.973 cm^2)

L = the distance of conduction path (20 cm)

A_B = the area of MAM baffle interior (0.0294 m^2)

A_o = the area of MAM baffle FOV opening (0.0022 m^2)

A_{ext} = the area of MAM baffle exterior (0.0301 m^2)

A_M = the area of MAM plate (0.00384 m^2)

$A_{int} = A_o - A_M$ (0.00182 m^2)

F_{B-M} = the view factor from baffle to MAM (0.0108)

F_{M-B} = the view factor from MAM to baffle (0.984)

F_{o-B} = the view factor from MAM baffle FOV to baffle barrel (0.8898)

ρ_M = the reflectivity of MAM (0.9)

ε_{int} = the emissivity of baffle interior (0.98)

ε_{ext} = the emissivity of baffle exterior (0.1, and 0.4)

ε_{sc} = the emissivity of spacecraft surface (0.1)

ε_M = the emissivity of MAM (0.3)

α_{ext} = the absorptivity of baffle exterior (0.4)

The total radiance including contributions from MAM plate and baffle, and the directly impinging solar radiance is described by

$$L = \rho_M E_{Mb}/\pi + \rho_M E_{sun} \cdot \eta \cdot A_M(t)/(\pi A_M)$$

$$+ \varepsilon_M \sigma T_M^4(t) A_M(t)/(\pi A_M) + \varepsilon_M \sigma T_{sc}^4 [1 - \frac{A_M(t)}{A_M}]/\pi \quad (20)$$

where

$$T_M(t) = \frac{1}{7} (\frac{t}{60}) + 283.16 \qquad 0 \leq t \leq 330$$

and

$$A_M(t) = A_M \cdot C(t)$$

where

$$C(t) = \frac{t}{60} \qquad \text{for } 0 \leq t \leq 60$$

$$C(t) = 1 \qquad \text{for } 61 \leq t \leq 270$$

$$C(t) = 5 - \frac{t-30}{60} \qquad \text{for } 271 \leq t \leq 330.$$

To be coupled with the equation for scanner baffle,

$$E_{source} = L \times 3.14159$$

4-3. A Simplified Model for a Scanner Baffle

Assuming that the scanner baffle is thermally well-connected to the scanner boxbeam, and a half of the baffle exterior is exposed to the solar flux and the spacecraft body, then the energy balance equation for the baffle can be written in a form (see Fig. 7)

$$\rho V c \dot{T}_b = A'_{exp} \cdot \alpha_b E_{sun} + A'_{exp} \varepsilon_{sc} \cdot \alpha_b \sigma T_{sc}^4 + F_{in\text{-}source} F_{ext\text{-}in} \alpha'_{in} E_{source} A''_{exp}$$

$$+ F_{ext\text{-}out} A_{out} \varepsilon_S \alpha_{in} \sigma T_S^4 - F_{in\text{-}ext} A_{in} \varepsilon_{in} \sigma T_b^4 - F_{out\text{-}ext} A_{out} \varepsilon_{out} \sigma T_b^4$$

$$- A_{ext} \cdot \varepsilon_b \sigma T_b^4 - \frac{kA}{L} (T_b - T_{sc}) \qquad (21)$$

where A_{ext} = the exterior area of scanner baffle (=41.9109 cm^2)

ρ = the density of the Al baffle barrel (=2.71 gr/cc)

c = the specific heat (=0.9 J/gr°C for Al)

V = the baffle volume (=2.3057 cm^3)

E_{sun} = the solar flux (=0.1351 W/cm^2)

σ = the Stefan-Boltzmann constant (=5.6698x10^{-12} W/cm^2K^4)

A'_{exp} = the exposure area (= $\frac{1}{2} A_{ext}$)

A''_{exp} = the exposure area to the source (= $\frac{3}{5} A_{ext}$)

A_{in} = the baffle FOV area (= 3.8353 cm^2)

A_{out} = the scanner FOV area (= 1.9478 cm^2)

A = the conduction-path area (=0.2820 cm^2)

L = the length between the center and edge (=2.4892 cm)

k = the thermal conductivity (= 1.56 W/cm°C)

T_{sc} = the spacecraft temperature (= -10 ~ 30 °C)

E_{source} = the source irradiance (= 0.0080 ~ 0.014 W/cm^2)

T_s = the scanner temperature (= 38°C)

T_b = instantaneous barrel temperature

T_{bo} = the baffle average temperature (= 10°C)

$F_{in\text{-}source}$ = the view factor between source and the opening of scanner baffle (= 0.94)

$F_{ext\text{-}in}$ = the view factor between baffle FOV and barrel (= 0.1265)

$F_{out\text{-}ext}$ = the view factor between scanner FOV and baffle barrel (= 0.984)

$F_{ext-out}$ = the view factor between baffle barrel and scanner FOV (= 0.0629)

F_{in-ext} = the view factor between barrel and baffle FOV (= 0.8735)

α_b = the baffle exterior absorptivity (= 0.1 ~ 0.8)

α_{in} = the barrel inside absorptivity (= 0.98)

α'_{in} = the barrel average absorptivity seen from the source (= 0.5)

ε_{sc} = the spacecraft emissivity (= 0.5)

ε_s = the scanner emissivity (= 0.9)

ε_{in} = the baffle interior emissivity (= 0.98)

$\varepsilon_{out} = \varepsilon_{in}$

ε_b = the baffle exterior emissivity (= 0.1 ~ 0.8)

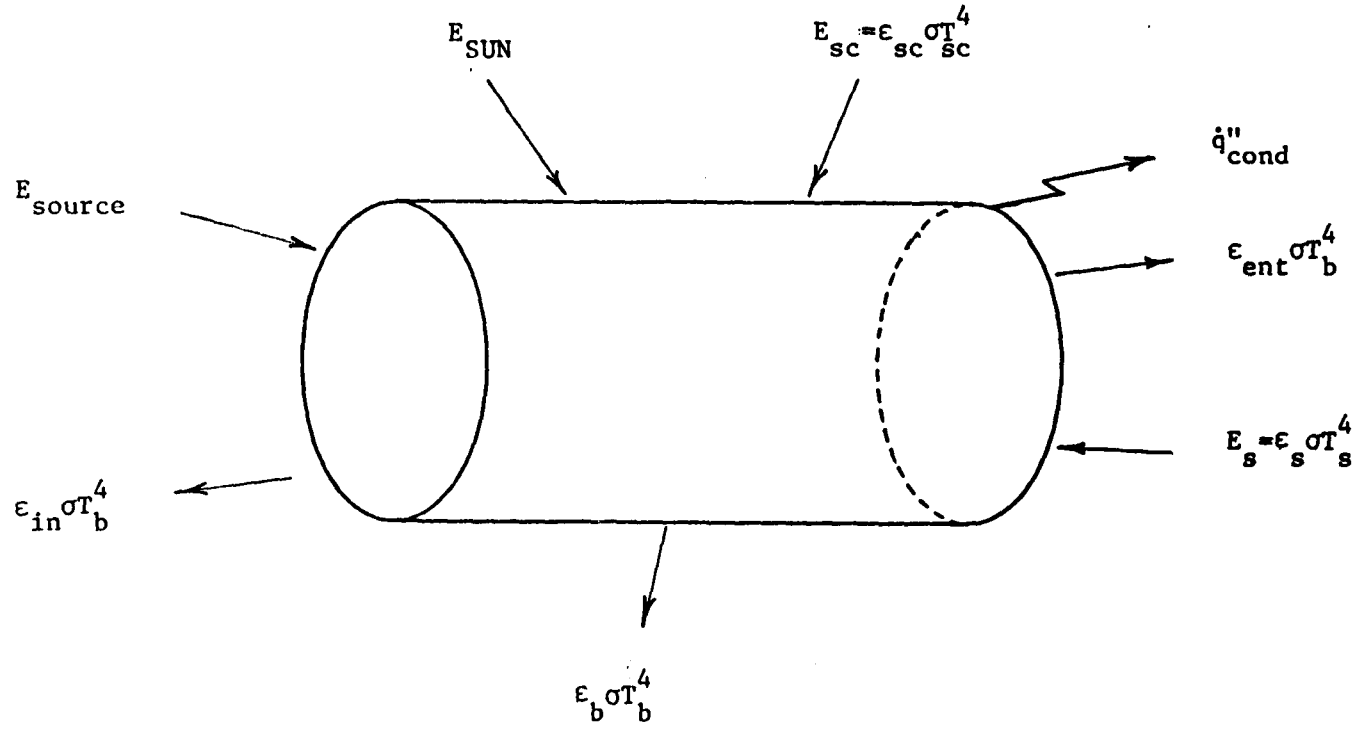

Figure 7. A Simple Diagram of a Scanner Baffle

Let $T_b^4 = (T_{bo} + \Delta T)^4$,

Then the above equation becomes

$$\dot{T}_b = \frac{1}{\rho Vc} \left\{ A'_{exp}\alpha_b E_{sun} + A'_{exp}\alpha_b \varepsilon_{sc}\sigma T_{sc}^4 + A''_{exp} F_{in\text{-}source} F_{ext\text{-}in} \alpha'_{in} E_{source} \right.$$

$$+ A_{out} F_{ext\text{-}out} \cdot \alpha_{in} \varepsilon_S \sigma T_s^4 - \frac{kA}{L} T_{sc} + 3A_{in\text{-}ext} \varepsilon_{in} \sigma T_{bo}^4$$

$$\left. + 3A_{out} F_{out\text{-}ext} \varepsilon_{out} \sigma T_{bo}^4 + 3A_{ext} \cdot e_b \sigma T_{bo}^4 \right\}$$

$$- \frac{1}{\rho Vc} \left\{ - \frac{kA}{L} + 4A_{in} F_{in\text{-}out} \varepsilon_{in} \sigma T_{bo}^3 + 4A_{out} F_{out\text{-}ext} \varepsilon_{out} \sigma T_{bo}^3 \right.$$

$$\left. + 4A_{ext} \varepsilon_b \sigma T_{bo}^3 \right\} T_b .$$

Let

$$P = \frac{1}{\rho Vc} \left\{ \frac{kA}{L} + 4\sigma T_{bo}^3 (A_{in} F_{in\text{-}ext} \varepsilon_{in} + A_{out} F_{out\text{-}out} \varepsilon_{out} + A_{ext} \varepsilon_b) \right\}$$

$$Q = \frac{1}{\rho Vc} \left\{ A'_{exp}\alpha_b E_{sun} + A'_{exp}\alpha_b \varepsilon_{sc}\sigma T_{sc}^4 + A''_{exp} F_{in\text{-}source} F_{ext\text{-}in} \alpha_{in} E_{source} \right.$$

$$+ A_{out} F_{ext\text{-}out} \alpha_{in} \varepsilon_s \sigma T_s^4 + \frac{kA}{L} T_{sc}$$

$$\left. + 3\sigma T_{bo}^4 (A_{in} F_{in\text{-}ext} \varepsilon_{in} + A_{out} F_{out\text{-}ext} \varepsilon_{out} + A_{ext} \varepsilon_b) \right\} .$$

Then the solution to the equation is

$$T_b = (T_{bo} - \frac{Q}{P}) e^{-Pt} + \frac{Q}{P} . \qquad (22)$$

Consequently, the radiant flux from the baffle to the scanner can be determined by

$$E_{FOV} = F_{out\text{-}b} \varepsilon_b \sigma T_b^4 . \qquad (23)$$

The amount of longwave contribution due to the change in the environmental conditions becomes

$$E_{FOV} = F_{out-b}\varepsilon_b\sigma(T_b^4 - T_{bo}^4) \quad . \tag{24}$$

These environmental conditions are the thermal coupling (k), the spacecraft temperature, T_{sc}, e.g., box beam or pedestal temperature which is probably determined by a cold orbit or a hot orbit, the source irradiance change during the day and night (E_{source}), the baffle exterior surface radiation parameters (α_b and ε_b), and the solar flux angle.

5. RESULTS AND DISCUSSIONS

Both TRY-I and II cases were interfaced with the scanner instrument simulation model for the total channel case to study the effects of varying the rate of housekeeping data (HKD) sampling on the count-output errors. Especially during the solar calibration, the MAM plate and baffle are heated and emit additional longwave radiation to the instrument. The magnitudes of these emitted energies from the MAM plate and baffle depend on various factors such as the conductivity between MAM baffle and spacecraft body, the radiative surface properties, and exposure area. The MAM plate and baffle both have a temperature probe and their temperature readings were originally designed to be transmitted down to the earth station every four second cycle. However, in an effort to decrease a persisting systematic noise (or called A-to-D noise), the HKD including these temperature readings were redesigned to be transmitted every 32 seconds (8 cycles) instead of every 4 second cycle. If the time interval between HKDs is large enough, so that the change of longwave emission from the MAM plate and baffle is not observed, then some errors will exist in the output counts in proportion to the magnitude of the longwave emission change. Accordingly, it is important to determine what interval of HKD is tolerable in order to avoid any significant errors if a noticeable error exists during a scan cycle.

To do this, in both TRY-I and II cases, the sun view was manipulated as

the following: A partial sun-view which is gradually increased to a full sun-view for 60 seconds, a full sun-view for 210 seconds, and again a partial sun-view which is in this case, gradually decreased to no sun-view for 60 seconds.

In TRY-I, to compute the emitted energy from the MAM plate and baffle, a linear approximation of the measured temperatures was used. The differences due to the approximation with respect to the real temperatures, were small.

However, the circumstances during solar calibration in orbit and in the ground calibration chamber are quite different. Accordingly in TRY-II, MAM baffle model as shown in the earlier section was to include possible radiation exchange with the environment.

Fig. 8 shows the solar radiance and the MAM baffle temperature variations during the solar calibration of 330 seconds for the TRY-II case. During the whole 330 second period, the MAM baffle temperature increases 2.75°K in TRY-I case and 9.44°K in TRY-II case. The solar radiance in Fig. 8 is a result of combining the directly impinging solar flux and the emitted radiations from the MAM plate and baffle. The same results can be found from Table I and II which show scanner baffle temperature, the MAM baffle temperature, the emitted energy from MAM baffle, the solar radiance, and the emitted radiant flux, E_{FOV}, from the scanner baffle for a part of a solar calibration. Table I shows results that considered the MAM plate and baffle heating to be solar flux while Table II shows results that excluded the MAM plate and baffle heating.

Fig. 9 shows the scanner baffle temperature, the emitted radiant flux from scanner baffle which falls onto the scanner, and the increment of radiant flux as based on a set temperature of 283.16°K when TRY-II case was employed.

Fig. 10 shows the increments of both the solar radiance and the emitted radiant flux from the scanner baffle when every 16 seconds data was plotted for 96 seconds with 70 seconds as a starting point during a full sun-view. The solid lines

signify the results considering the MAM plate and baffle heating by solar flux and the broken lines excluding the MAM plate and the baffle heating. During a 32 second period, the increment of solar radiance is about 1.5 $W/m^2 \cdot sr$ (see the second solid line from the top) which is equivalent to 9 counts. During one scan cycle, the solar radiance varies about 0.17 $W/m^2 \cdot sr$ which is within an acceptable range (presumably 0.3 $W/m^3 \cdot sr$ per cycle).

In both TRY-I and II cases, the temperature increments during an increasing partial (60 seconds) through a full (210 seconds) to a diminishing partial (60 seconds) sun-views were 2.75°K and 9°K, respectively. During one scan cycle in a full sun-view, the total radiance increments are about 0.055 $W/m^2 \cdot sr$ for TRY-I case and 0.17 $W/m^2 \cdot sr$ for TRY-II case. These results are due to the longwave contributions reflected and emitted from the MAM plate and baffle.

The scanner simulation model, when it was coupled with TRY-I and II cases, shows that the count output increments are about 1 count for TRY-I and about 1.5 count for TRY-II. These count increments are equivalent to about 0.17 $W/m^2 \cdot sr$ and 0.26 $W/m^2 \cdot sr$ radiance increments respectively, if 1 $W/m^2 \cdot sr$ is equivalent to 6 counts. In this computation, the scanner simulation model was integrated with the scanner baffle model. The differences would be due mainly to the emitted radiant flux E_{FOV} from the scanner baffle. The radiance equivalent to the emitted radiant flux increment, ΔE_{FOV}, from the scanner baffle was about 0.09 $W/m^2 \cdot sr$ per scan cycle. The emitted radiant flux E_{FOV} from the scanner baffle was estimated by setting the MAM plate and baffle temperature at 283.16°K.

Accordingly, eliminating the ΔE_{FOV} effect which occurs by as much as ~ 0.55 counts when the scanner simulation model was coupled with TRY-I and II, the actual output incurements per scan cycle was 0.45 and 0.95 counts for TRY-I and II, respectively. Because the count difference between the source and spacelooks is used in the count conversion procedure, the elimination of ΔE_{FOV} which is almost the same

during a scan period, would not cause any significant errors.

As a whole, any difference attributed to the MAM plate and baffle temperature variations has a negligible effect on the input radiation field impinging on the instrument field-of-view limiter.

6. RECOMMENDATION

The results from the above analysis show that the heat input variations due largely to the solar radiance and irradiance during a scan cycle are small.

Hence, it is certain that a 32 second HKD acquisition interval as opposed to every 4 seconds, should not significantly affect the estimation of a radiation field in the field-of-view of a scanner instrument unless unknown factors disturb the radiation field and thermal loadings.

7. REFERENCES

1. Hendricks, C. K., "Final Calibration Report on ERBE Protoflight Model Scanner Instrument", NO. D06905, August 15, 1984.

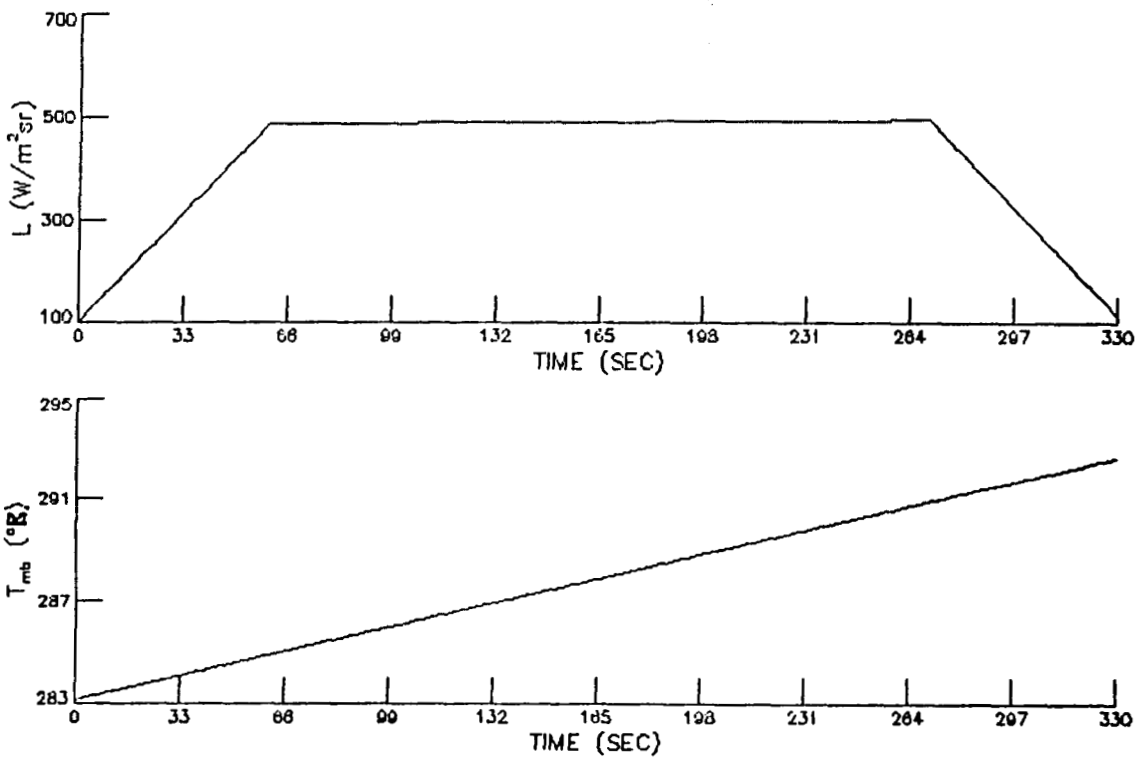

Figure 8. Input Radiance and MAM Baffle Temperature Variations during 330 second Solar Calibration (both ends show the partial sun-view).

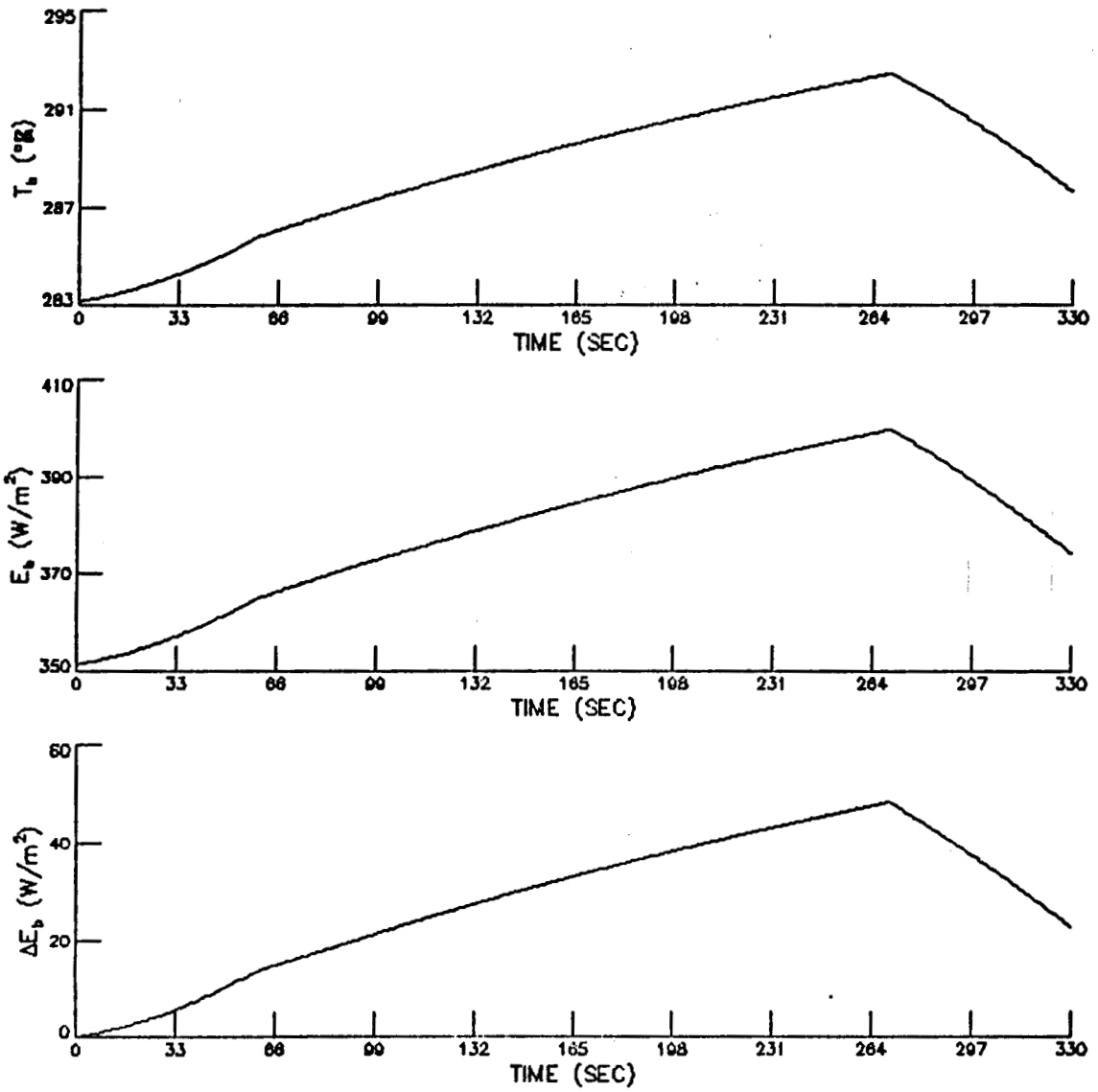

Figure 9. Scanner Baffle Temperature, Irradiation, E_{FOV}, from Scanner Baffle and net increment of E_{FOV} during 330 second Solar Calibration.

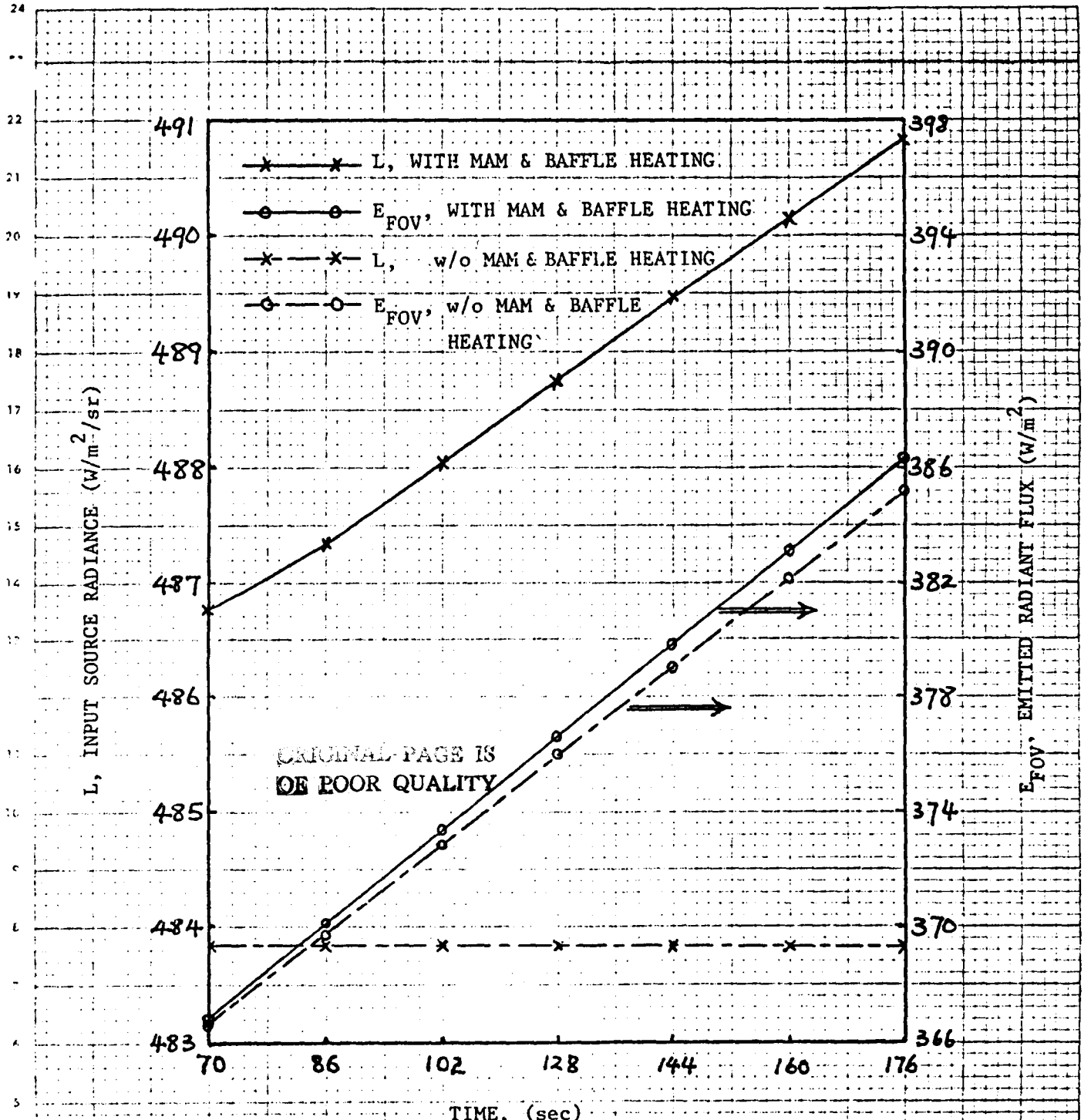

Figure 10. Input Source Radiance, L, and Irradiance, E_{FOV}, Variations with and without MAM & BAFFLE HEATING during a full Sun-view Measurement (TRY-II case).

TABLE I. RADIATION FIELD WITH EMISSIONS FROM MAM PLATE AND BAFFLE

TIME (sec)	SCANNER BAFFLE TEMPERATURE (^{o}K)	MAM BAFFLE TEMPERATURE (^{o}K)	EMITTED FLUX FROM MAM BAFFLE (W/m^2)	SOLAR RADIANCE ($W/m^2.sr$)	E_{FOV} (W/m^2)
40	TB=284.584	TMB=284.269	EMB=357.024	L=351.348	EB=358.609
41	TB=284.636	TMB=284.297	EMB=357.167	L=357.776	EB=358.874
42	TB=284.689	TMB=284.326	EMB=357.310	L=364.205	EB=359.143
43	TB=284.743	TMB=284.354	EMB=357.453	L=370.633	EB=359.415
44	TB=284.798	TMB=284.383	EMB=357.597	L=377.061	EB=359.692
45	TB=284.854	TMB=284.411	EMB=357.740	L=383.489	EB=359.972
46	TB=284.910	TMB=284.440	EMB=357.883	L=389.918	EB=360.256
47	TB=284.967	TMB=284.468	EMB=358.026	L=396.346	EB=360.544
48	TB=285.025	TMB=284.496	EMB=358.170	L=402.775	EB=360.836
49	TB=285.083	TMB=284.525	EMB=358.313	L=409.203	EB=361.132
50	TB=285.142	TMB=284.553	EMB=358.456	L=415.632	EB=361.432
51	TB=285.202	TMB=284.582	EMB=358.600	L=422.061	EB=361.735
52	TB=285.263	TMB=284.610	EMB=358.743	L=428.489	EB=362.043
53	TB=285.324	TMB=284.639	EMB=358.887	L=434.918	EB=362.354
54	TB=285.386	TMB=284.667	EMB=359.031	L=441.347	EB=362.669
55	TB=285.449	TMB=284.696	EMB=359.174	L=447.776	EB=362.988
56	TB=285.512	TMB=284.724	EMB=359.318	L=454.205	EB=363.311
57	TB=285.576	TMB=284.753	EMB=359.462	L=460.634	EB=363.637
58	TB=285.641	TMB=284.781	EMB=359.606	L=467.063	EB=363.967
59	TB=285.706	TMB=284.810	EMB=359.750	L=473.492	EB=364.302
60	TB=285.773	TMB=284.838	EMB=359.893	L=479.921	EB=364.639
61	TB=285.839	TMB=284.867	EMB=360.037	L=486.350	EB=364.981
62	TB=285.881	TMB=284.895	EMB=360.182	L=486.392	EB=365.191
63	TB=285.921	TMB=284.924	EMB=360.326	L=486.435	EB=365.400
64	TB=285.962	TMB=284.952	EMB=360.470	L=486.477	EB=365.608
65	TB=286.003	TMB=284.981	EMB=360.614	L=486.520	EB=365.817
66	TB=286.044	TMB=285.009	EMB=360.758	L=486.562	EB=366.024
67	TB=286.084	TMB=285.038	EMB=360.902	L=486.605	EB=366.232
68	TB=286.124	TMB=285.066	EMB=361.047	L=486.647	EB=366.438
69	TB=286.165	TMB=285.095	EMB=361.191	L=486.690	EB=366.645
70	TB=286.205	TMB=285.123	EMB=361.336	L=486.732	EB=366.851
71	TB=286.245	TMB=285.152	EMB=361.480	L=486.775	EB=367.056
72	TB=286.285	TMB=285.180	EMB=361.625	L=486.818	EB=367.261
73	TB=286.325	TMB=285.209	EMB=361.769	L=486.860	EB=367.465
74	TB=286.364	TMB=285.237	EMB=361.914	L=486.903	EB=367.669
75	TB=286.404	TMB=285.266	EMB=362.059	L=486.945	EB=367.873
76	TB=286.443	TMB=285.294	EMB=362.203	L=486.988	EB=368.076
77	TB=286.483	TMB=285.323	EMB=362.348	L=487.031	EB=368.278
78	TB=286.522	TMB=285.351	EMB=362.493	L=487.073	EB=368.480
79	TB=286.561	TMB=285.380	EMB=362.638	L=487.116	EB=368.682
80	TB=286.600	TMB=285.408	EMB=362.783	L=487.159	EB=368.883
81	TB=286.639	TMB=285.437	EMB=362.928	L=487.201	EB=369.084
82	TB=286.678	TMB=285.465	EMB=363.073	L=487.244	EB=369.284
83	TB=286.717	TMB=285.494	EMB=363.218	L=487.287	EB=369.484
84	TB=286.756	TMB=285.522	EMB=363.363	L=487.330	EB=369.683
85	TB=286.794	TMB=285.551	EMB=363.508	L=487.372	EB=369.882
86	TB=286.833	TMB=285.579	EMB=363.653	L=487.415	EB=370.080
87	TB=286.871	TMB=285.608	EMB=363.799	L=487.458	EB=370.278
88	TB=286.909	TMB=285.636	EMB=363.944	L=487.501	EB=370.475

TABLE II. RADIATION FIELD WITHOUT EMISSIONS FROM MAM PLATE AND BAFFLE

TIME (sec)	SCANNER BAFFLE TEMPERATURE (^{o}K)	MAM BAFFLE TEMPERATURE (^{o}K)	EMITTED FLUX FROM MAM BAFFLE (W/m^2)	SOLAR RADIANCE ($W/m^2.sr$)	E_{FOV} (W/m^2)
40	TB=284.579	TMB=283.160	EMB=351.487	L=349.732	EB=358.587
41	TB=284.632	TMB=283.160	EMB=351.487	L=356.118	EB=358.850
42	TB=284.685	TMB=283.160	EMB=351.487	L=362.503	EB=359.118
43	TB=284.738	TMB=283.160	EMB=351.487	L=368.889	EB=359.389
44	TB=284.793	TMB=283.160	EMB=351.487	L=375.275	EB=359.664
45	TB=284.848	TMB=283.160	EMB=351.487	L=381.660	EB=359.943
46	TB=284.904	TMB=283.160	EMB=351.487	L=388.046	EB=360.226
47	TB=284.961	TMB=283.160	EMB=351.487	L=394.432	EB=360.513
48	TB=285.018	TMB=283.160	EMB=351.487	L=400.817	EB=360.804
49	TB=285.076	TMB=283.160	EMB=351.487	L=407.203	EB=361.098
50	TB=285.135	TMB=283.160	EMB=351.487	L=413.588	EB=361.397
51	TB=285.195	TMB=283.160	EMB=351.487	L=419.974	EB=361.699
52	TB=285.255	TMB=283.160	EMB=351.487	L=426.360	EB=362.005
53	TB=285.316	TMB=283.160	EMB=351.487	L=432.745	EB=362.315
54	TB=285.378	TMB=283.160	EMB=351.487	L=439.131	EB=362.628
55	TB=285.440	TMB=283.160	EMB=351.487	L=445.516	EB=362.945
56	TB=285.503	TMB=283.160	EMB=351.487	L=451.902	EB=363.266
57	TB=285.567	TMB=283.160	EMB=351.487	L=458.288	EB=363.591
58	TB=285.632	TMB=283.160	EMB=351.487	L=464.673	EB=363.920
59	TB=285.697	TMB=283.160	EMB=351.487	L=471.059	EB=364.252
60	TB=285.763	TMB=283.160	EMB=351.487	L=477.444	EB=364.588
61	TB=285.829	TMB=283.160	EMB=351.487	L=483.830	EB=364.928
62	TB=285.870	TMB=283.160	EMB=351.487	L=483.830	EB=365.136
63	TB=285.910	TMB=283.160	EMB=351.487	L=483.830	EB=365.344
64	TB=285.951	TMB=283.160	EMB=351.487	L=483.830	EB=365.550
65	TB=285.991	TMB=283.160	EMB=351.487	L=483.830	EB=365.757
66	TB=286.032	TMB=283.160	EMB=351.487	L=483.830	EB=365.963
67	TB=286.072	TMB=283.160	EMB=351.487	L=483.830	EB=366.168
68	TB=286.112	TMB=283.160	EMB=351.487	L=483.830	EB=366.373
69	TB=286.152	TMB=283.160	EMB=351.487	L=483.830	EB=366.577
70	TB=286.191	TMB=283.160	EMB=351.487	L=483.830	EB=366.781
71	TB=286.231	TMB=283.160	EMB=351.487	L=483.830	EB=366.985
72	TB=286.271	TMB=283.160	EMB=351.487	L=483.830	EB=367.188
73	TB=286.310	TMB=283.160	EMB=351.487	L=483.830	EB=367.390
74	TB=286.349	TMB=283.160	EMB=351.487	L=483.830	EB=367.592
75	TB=286.389	TMB=283.160	EMB=351.487	L=483.830	EB=367.793
76	TB=286.428	TMB=283.160	EMB=351.487	L=483.830	EB=367.994
77	TB=286.467	TMB=283.160	EMB=351.487	L=483.830	EB=368.195
78	TB=286.506	TMB=283.160	EMB=351.487	L=483.830	EB=368.395
79	TB=286.544	TMB=283.160	EMB=351.487	L=483.830	EB=368.594
80	TB=286.583	TMB=283.160	EMB=351.487	L=483.830	EB=368.793
81	TB=286.621	TMB=283.160	EMB=351.487	L=483.830	EB=368.991
82	TB=286.660	TMB=283.160	EMB=351.487	L=483.830	EB=369.189
83	TB=286.698	TMB=283.160	EMB=351.487	L=483.830	EB=369.387
84	TB=286.736	TMB=283.160	EMB=351.487	L=483.830	EB=369.584
85	TB=286.775	TMB=283.160	EMB=351.487	L=483.830	EB=369.780
86	TB=286.813	TMB=283.160	EMB=351.487	L=483.830	EB=369.976
87	TB=286.850	TMB=283.160	EMB=351.487	L=483.830	EB=370.172
88	TB=286.888	TMB=283.160	EMB=351.487	L=483.830	EB=370.367

TABLE III. RESULTS OF TRY-I AND II CASES WHILE FULL SUN-VIEW

TRY-I CASE				TRY-II CASE		
TIME	L	E_{FOV}	COUNTS*	L	E_{FOV}	COUNTS*
70	478.94	366.78	2902.2	486.80	366.85	2944.4
74	478.99	367.59	2903.5	486.97	367.67	2946.4
78	479.04	368.40	2904.8	487.14	368.48	2948.3
82	479.10	369.19	2905.9	487.32	369.28	2950.1
86	479.15	369.98	2907.0	487.49	370.08	2951.8
90	479.20	370.76	2908.0	487.66	370.87	2953.5
94	479.25	371.53	2909.0	487.84	371.05	2955.2
98	479.32	372.29	2910.1	488.01	372.43	2956.9
102	479.35	373.05	2911.2	488.18	373.19	2958.7
106	479.41	373.80	2912.2	488.36	373.95	2960.4
110	479.46	374.54	2913.2	488.53	374.71	2962.1
114	479.51	375.27	2914.2	488.70	375.45	2963.7
118	479.56	376.00	2915.2	488.88	376.19	2965.4
122	479.61	376.72	2916.2	489.05	376.92	2967.0
126	479.66	377.43	2917.2	489.23	377.65	2968.7
130	479.72	378.14	2918.1	489.40	378.37	2970.3
134	479.77	378.83	2919.1	489.58	379.08	2971.9
138	479.82	379.52	2920.0	489.76	379.78	2973.6
142	479.87	380.21	2920.9	489.93	380.48	2975.2
146	479.92	380.89	2921.9	490.11	381.17	2976.8
150	479.98	381.56	2922.8	490.28	381.86	2978.4
154	480.03	382.22	2923.7	490.46	382.54	2980.0
158	480.08	382.88	2924.6	490.64	383.21	2981.5
162	480.13	383.53	2925.5	490.81	383.88	2983.1
166	480.18	384.17	2926.4	290.99	384.54	2984.7

*Simulation results - Gain factor may not be correct.

Standard Bibliographic Page

1. Report No. NASA CR-178294	2. Government Accession No.	3. Recipient's Catalog No.
4. Title and Subtitle Development of Response Models for the Earth Radiation Budget Experiment (ERBE) Sensors: Part III - ERBE Scanner Measurement Accuracy Analysis Due to Reduced Housekeeping Data		5. Report Date March 20, 1987 6. Performing Organization Code
7. Author(s) Sang H. Choi, Dan A. Chrisman, Jr., Nesim Halyo		8. Performing Organization Report No. FR 687105
9. Performing Organization Name and Address Information & Control Systems, Incorporated 28 Research Drive Hampton, VA 23666		10. Work Unit No. 665-45-30-01 11. Contract or Grant No. NAS1-16130
12. Sponsoring Agency Name and Address National Aeronautics and Space Administration Langley Research Center Hampton, VA 23665		13. Type of Report and Period Covered Contractor Report 14. Sponsoring Agency Code

15. Supplementary Notes

Langley Technical Monitor: Robert J. Keynton

Final Report

16. Abstract

The accuracy of scanner measurements was evaluated when the sampling frequency of sensor housekeeping (HK) data was reduced from once every scan to once every eight scans. The resulting increase in uncertainty was greatest for sources with rapid or extreme temperature changes. In this analysis, we focused on the Mirror Attenuator Mosaic (MAM) baffle and plate and scanner radiometer baffle due to their relatively high temperature changes during solar calibrations. Since only solar simulator data was available, we approximated the solar temperatures on these components and the radiative and thermal gradients in the MAM baffle due to reflected sunlight.

Of the two cases we considered for the MAM plate and baffle temperatures, one uses temperatures obtained from the ground calibration. The other attempt uses temperatures computed from the MAM baffle model.

This analysis shows that the heat input variations due largely to the solar radiance and irradiance during a scan cycle are small. It also demonstrates that reasonable intervals longer than the current HK data acquisition interval should not significantly affect the estimation of a radiation field in the sensor field-of-view.

17. Key Words (Suggested by Authors(s))	18. Distribution Statement
Scanner, Accuracy Analysis, Housekeeping Data, Mirror Attenuator Mosaic, Solar Calibrations, Data Acquisition Interval	Unclassified - Unlimited Subject Category 35

19. Security Classif.(of this report)	20. Security Classif.(of this page)	21. No. of Pages	22. Price
Unclassified	Unclassified	44	A03

For sale by the National Technical Information Service, Springfield, Virginia 22161

NASA Langley Form 63 (June 1985)